Check for updates

Advanced Functional Materials

ADVANCED FUNCTIONAL MATERIALS
www.afm-journal.de

RESEARCH ARTICLE

Bias-Free Tactile Synaptic Ionogel With Viscoelastic Memory for Biomechanical Monitoring

Nan Wang[1] | Yan Yan[1] | Mingqi Ding[1] | Yuxuan Zhang[1] | Mengxi Gu[2] | Jie Zhou[1] | Wu Guo[3] | Haoran Pei[3] | Bowen Li[1,4] | Quan Quan[1] | Yu Song[2] | Johnny C. Ho[1,4,5,6]

[1]Department of Materials Science and Engineering, City University of Hong Kong, Kowloon, Hong Kong, China | [2]Department of Biomedical Engineering, City University of Hong Kong, Kowloon, Hong Kong, China | [3]National Key Laboratory of Advanced Polymer Materials, Polymer Research Institute of Sichuan University, Chengdu, China | [4]Shenzhen Research Institute, City University of Hong Kong, Shenzhen, China | [5]State Key Laboratory of Terahertz and Millimeter Waves, City University of Hong Kong, Hong Kong SAR, China | [6]Institute For Materials Chemistry and Engineering, Kyushu University, Fukuoka, Japan

Correspondence: Yu Song (yusong@cityu.edu.hk) | Johnny C. Ho (johnnyho@cityu.edu.hk)

Received: 5 July 2026 | **Revised:** 3 September 2026 | **Accepted:** 23 September 2026

Keywords: bias-free neuromorphic computing | biomechanical monitoring | piezoionic tactile synapses | self-healing ionogels | viscoelastic ion-trapping

ABSTRACT

Endowing artificial skins with adaptation and sensory memory is essential for intelligent tactile perception. However, conventional transistor-based neuromorphic systems rely on energy-intensive, decoupled architectures that fundamentally constrain their structural flexibility and energy efficiency. In this study, we report a monolithic, bias-free piezoionic tactile synapse that exhibits adaptive plasticity driven solely by mechanical stimuli. Learning and memory arise from stress-induced piezoelectric polarization at the dynamic interface, which drives rapid ion separation, coupled with supramolecular confinement within the viscoelastic polymer network that retards cation backflow. This kinematic asymmetry induces pronounced ion transport hysteresis, directly translating mechanical inputs into cumulative postsynaptic potentials. Furthermore, the supramolecular network inherently affords autonomous self-healing and conformal adhesion. Leveraging these features, we demonstrate a self-powered electronic skin for the in situ quantification of neuromuscular coordination and biomechanical endurance. By unifying mechanotransduction and memory at the material level, this work establishes a novel paradigm for energy-efficient biological-machine interfaces.

1 | Introduction

Artificial synapses that emulate the dynamic signal modulation of biological neural networks offer a transformative approach to integrating sensing, memory, and processing capabilities within a single architecture [1, 2]. Among human sensory modalities, tactile perception is fundamental for decoding the external environment and underpinning adaptive motor control. Biologically, perceptual awareness arises from the synaptic preprocessing of action potentials generated by mechanoreceptors, including integration, threshold filtering, and feature encoding [3–5]. While recent synthetic materials, such as soft hydrogels, successfully mimic the detecting modalities of human skin, their capacity to emulate the complex information processing of neural networks remains severely limited [6–8]. Endowing artificial skins with such spatiotemporal adaptation and memory is crucial for advancing intelligent tactile systems in next-generation wearable healthcare and robotic perception [9, 10].

State-of-the-art neuromorphic tactile systems typically employ a decoupled architecture, spatially separating mechanoreceptors from synaptic signal generators, thereby necessitating complex

All rights reserved, including rights for text and data mining and training of artificial intelligence technologies or similar technologies.
© 2026 Wiley-VCH GmbH

intermediate signal transduction [11–13]. Most existing tactile sensory systems rely on transistor architectures to achieve synaptic plasticity, in which postsynaptic currents are modulated by gate-induced changes in source-drain channel conductivity [14–16]. Although these devices exhibit promising performance, this indirect transduction introduces risks of signal distortion, loss, and latency due to complex chain processes, such as charge injection, ion migration, and polarization switching [17–20]. More critically, transistor-based architectures inherently require high power consumption and external biasing voltages (e.g., in floating-gate variants) to drive information processing [21, 22]. Consequently, their reliance on complex external circuitry severely limits their ability to achieve the autonomous, dynamic signal modulation characteristic of biological synapses.

In this study, we report a monolithic, self-powered piezoionic tactile synapse driven by an asymmetric ion-trapping mechanism. The tactile ionogel is fabricated via the in situ polymerization of a polymerizable deep eutectic solvent (PDES) on vertically grown Tellurium nanowires (Te NWs). This composite features a dynamic ion-sieving interface in which strong anion-dipole interactions govern ion distribution and selective transport. Mechanical stimuli induce piezoelectric polarization in the Te NWs, driving rapid charge separation, while the viscoelastic memory of the polymer network constrains cation backflow through reversible hydrogen bonding. This decoupled kinematic asymmetry facilitates bias-free signal accumulation, enabling the generation of adaptive synaptic outputs purely from mechanical inputs. Concurrently, the abundant non-covalent network confers exceptional mechanical adaptability and autonomous self-healing. We validate the potential of this tactile synapse for intelligent sensing in biomechanical monitoring, successfully quantifying motion quality and neuromuscular coordination during rehabilitation tasks. This work provides a robust material-level strategy for bias-free neuromorphic computing, advancing the development of associative learning-enabled electronic skins.

2 | Results

2.1 | Bioinspired Architecture of a Zero-Power Piezoionic Tactile Synapse

The human brain encodes and stores information through persistent, activity-dependent plasticity at synaptic connections [23]. Biologically, this process is governed by controlled ion transport across cell membranes, in which interaction-gated ion channels mediate selectivity, adaptation, and gain modulation of sensory inputs [24, 25]. For instance, neurotransmitters such as glutamate bind to postsynaptic receptors via electrostatic interactions and hydrogen bonding, triggering selective ion fluxes that induce membrane depolarization and modulate sensory signaling [26, 27] (Figure 1a). Translating this biological paradigm into human-machine interfaces and health-monitoring systems requires transcending simple mechanoelectrical transduction toward autonomous, intelligent information processing (Figure 1b).

Drawing inspiration from this dynamic biological paradigm, we developed a zero-power tactile ionogel with built-in learning and adaptive functions by engineering ion-selective channels coupled with asymmetric recovery pathways. We selected a polymerizable deep eutectic solvent (PDES) as the ionic carrier matrix for its solvent-free tunable viscoelasticity and high density of mobile charge carriers [28, 29]. The matrix is copolymerized from acrylic acid (AA), maleic anhydride (MA), and N-methylmaleamic acid (NMA), which act as hydrogen bond donors, with choline chloride (ChCl) serving as the acceptor. When the PDES precursor is polymerized in situ on vertically grown Te NWs [30], a self-adaptable ionic double layer (IDL) forms at the organic-inorganic interface (Figure 1c). The multiscale Te NWs (10–50 μm) facilitate deep precursor infiltration. At the same time, their extensive high surface area provides abundant active sites for supramolecular assembly and selective stabilization of chloride (Cl^-) via strong anion-dipole interactions (Figure 1d).

More critically, as piezoelectric semiconductors, Te nanowires exhibit a synergistic piezo-ionic effect [30–32]. As shown in Figure 1e, we analyzed the polarization characteristics of the Te NWs, pristine PDES, and the composite ionogel using piezoelectric charge coefficient (d_{33}) measurements. Vertically aligned Te NWs exhibit a negative d_{33} coefficient, indicating an axial built-in polarization field (E_{pz}) directed from the non-pressed to the pressed surface upon compression. This E_{pz} creates a strong electrostatic attraction for polymeric anions at the interface. Conversely, pristine PDES displays a positive d_{33} coefficient, attributed to the pressure-driven mobility of Cl^- ions, which possess a smaller free volume than cations. Upon integration, the built-in field is distinctly reversed and intensified, indicating that the positively polarized Te interface effectively immobilizes Cl^- anions through strong ion-dipole interactions. This interfacial redistribution establishes the foundation for asymmetric ion migration: mechanical stimuli rapidly drive free $[Ch]^+$ cations released from the IDL into the polymer bulk, generating an immediate electrical response. Upon pressure release, the robust viscoelastic memory of the PDES matrix and reversible hydrogen bonding severely hinder the backflow of $[Ch]^+$. This "ion-trapping" dynamically maintains electrical memory across successive stimuli, thereby emulating short-term potentiation (STP) in biological synapses [34, 35].

2.2 | Pressure-Gated Ion Migration Driven by Dynamic Interfacial Bonding

Abundant supramolecular interaction sites drive the intimate interpenetration of PDES and Te nanowires. Figure 2a depicts the ion-dipole interactions at the organic-inorganic interface and the extensive hydrogen-bonding network within the polymer matrix. To elucidate the pressure-driven ion migration mechanism and underlying supramolecular interactions, we conducted spectroscopic characterization and molecular dynamics (MD) simulations. As shown in Figure 2b, the peak in the Raman spectrum located at 120 cm^{-1} is identified as the characteristic absorption of Te, corresponding to the symmetric stretching vibration of the 1D nanochain [33]. The region fitted to two peaks at 700 and 740 cm^{-1} is assigned to $-C-N^+-$ vibrations of quaternary ammonium salts, representing free Choline cations (F1) and bound Choline cations (F2), respectively (Figure 2c). Notably, incorporating Te NWs

16163028, 2026, 90, Downloaded from https://advanced.onlinelibrary.wiley.com/doi/10.1002/adfm.78811 by Yu Song - City University Of Hong Kong , Wiley Online Library on [10/11/2026]. See the Terms and Conditions (https://onlinelibrary.wiley.com/terms-and-conditions) on Wiley Online Library for rules of use; OA articles are governed by the applicable Creative Commons License

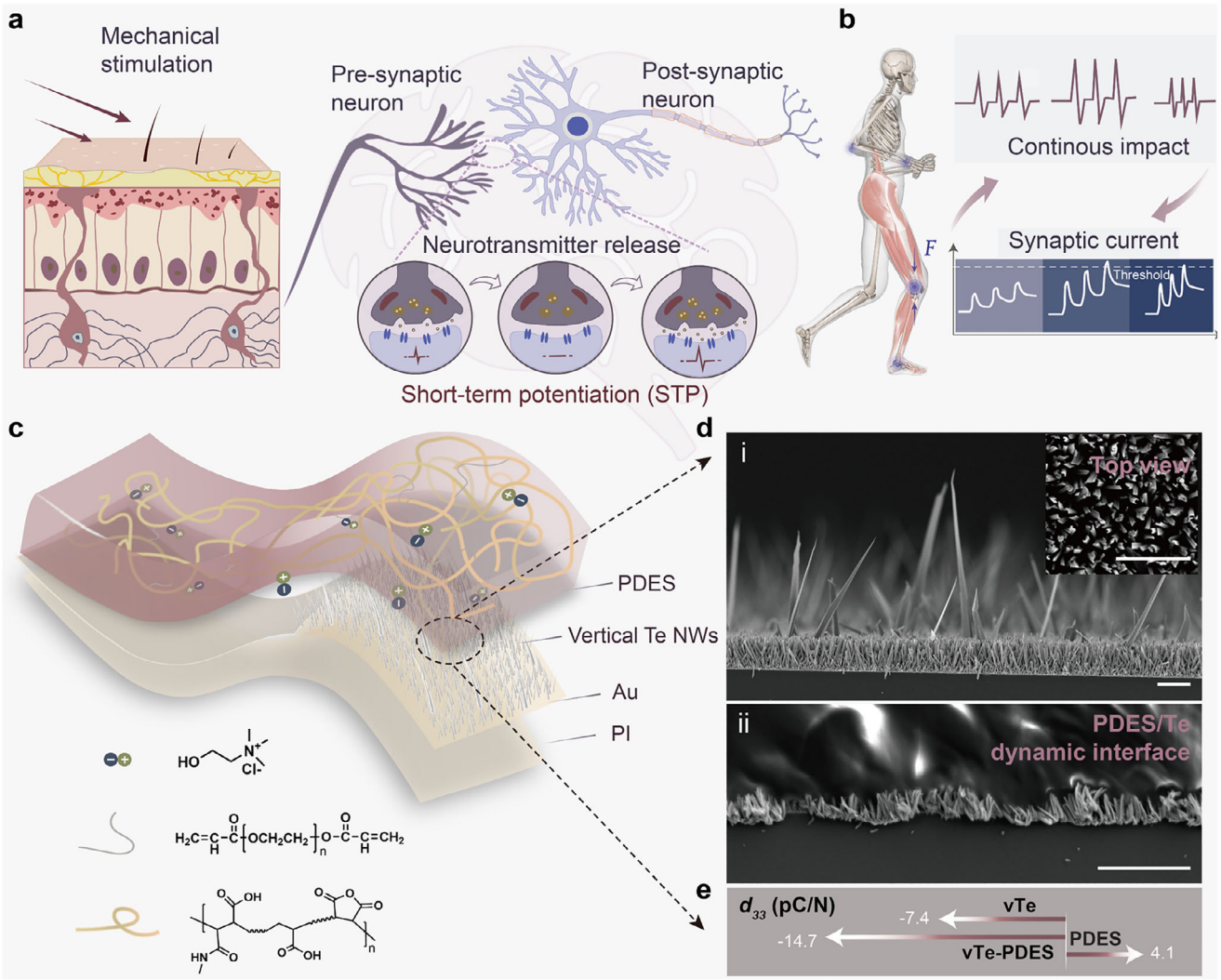


FIGURE 1 | Bioinspired architecture of a bias-free piezoionic tactile synapse. (a) Schematic illustrating the role of synaptic connections in biological tactile perception, where mechanoreceptors transmit stimuli to neurons for processing via synaptic plasticity. (b) Conceptual illustration of intelligent tactile sensing. Unlike conventional sensors with transient responses, the tactile synapse accumulates signals under continuous impact, mimicking the adaptivity of neuromuscular systems to sustained stimuli. (c) Structural schematic of the vTe-PDES ionogel. (d) SEM images of (i) Surface and cross-sectional morphology of vertically grown Te NWs and (ii) Cross-section of the organic-inorganic dynamic interface. Scale bar: 20 μm. (e) Comparison of piezoelectric coefficients (d_{33}) for Te NWs, pristine PDES, and the vTe-PDES composite.

into the PDES ionogel increases the proportion of the F1 peak area, indicating that the Te surface effectively sequesters Cl^- anions, thereby weakening the electrostatic confinement of choline cations and enhancing their mobility [34]. This interfacial ion-sieving effect establishes the chemical foundation for pressure-driven ion convection. Moreover, the intensity of the symmetric stretching vibration of the carboxylate group (COO^-, 1400–1450 cm^{-1}) decreases after compositing (Figure S1), which is attributed to a dipole interaction between Te and the C═O bond. This redistribution of the electron cloud reduces the group's vibrational activity, further demonstrating the formation of the interfacial dynamic bond network.

Perturbation-correlation moving-window (PCMW) analysis further visualizes the reversible dissociation-reassociation dynamics of the supramolecular crosslinks under stress. Continuous spectral shifts in the broad O–H/N–H stretching envelope (3600–2900 cm^{-1}) and in the C═O stretching mode (~1700 cm^{-1}) confirm the pronounced pressure-responsiveness of the hydrogen-bonded network (Figure S2). Driven by mechanical compression, the unconfined $[Ch]^+$ cations undergo directional migration. As pressure increases, cations first aggregate briefly at the pressurized terminal due to deformation, increasing local concentration. They then gradually approach the unpressurized terminal and reach the threshold, as evidenced by two extreme values around 8 and 15 N in the PCMW asynchronous maps (Figure 2d). 2D correlation spectroscopy (2D COS) provides additional insight into the sequential movement behavior of $[Ch]^+$ cations. According to Noda's rule, the response sequence of the free $[Ch]^+$ cations at 1180 cm^{-1} is before the bound $[Ch]^+$ cations at 1120 cm^{-1} (Figure 2e) [35, 36]. This temporal sequence is consistent with the macroscopic synaptic piezoionic response, in which an initial rapid voltage spike is driven by free cations, followed by a sustained voltage accumulation as the depletion of free cations near the interface shifts the free-bound equilibrium and progressively

16163028, 2026, 90, Downloaded from https://advanced.onlinelibrary.wiley.com/doi/10.1002/adfm.78811 by Yu Song - City University Of Hong Kong , Wiley Online Library on [10/11/2026]. See the Terms and Conditions (https://onlinelibrary.wiley.com/terms-and-conditions) on Wiley Online Library for rules of use; OA articles are governed by the applicable Creative Commons License

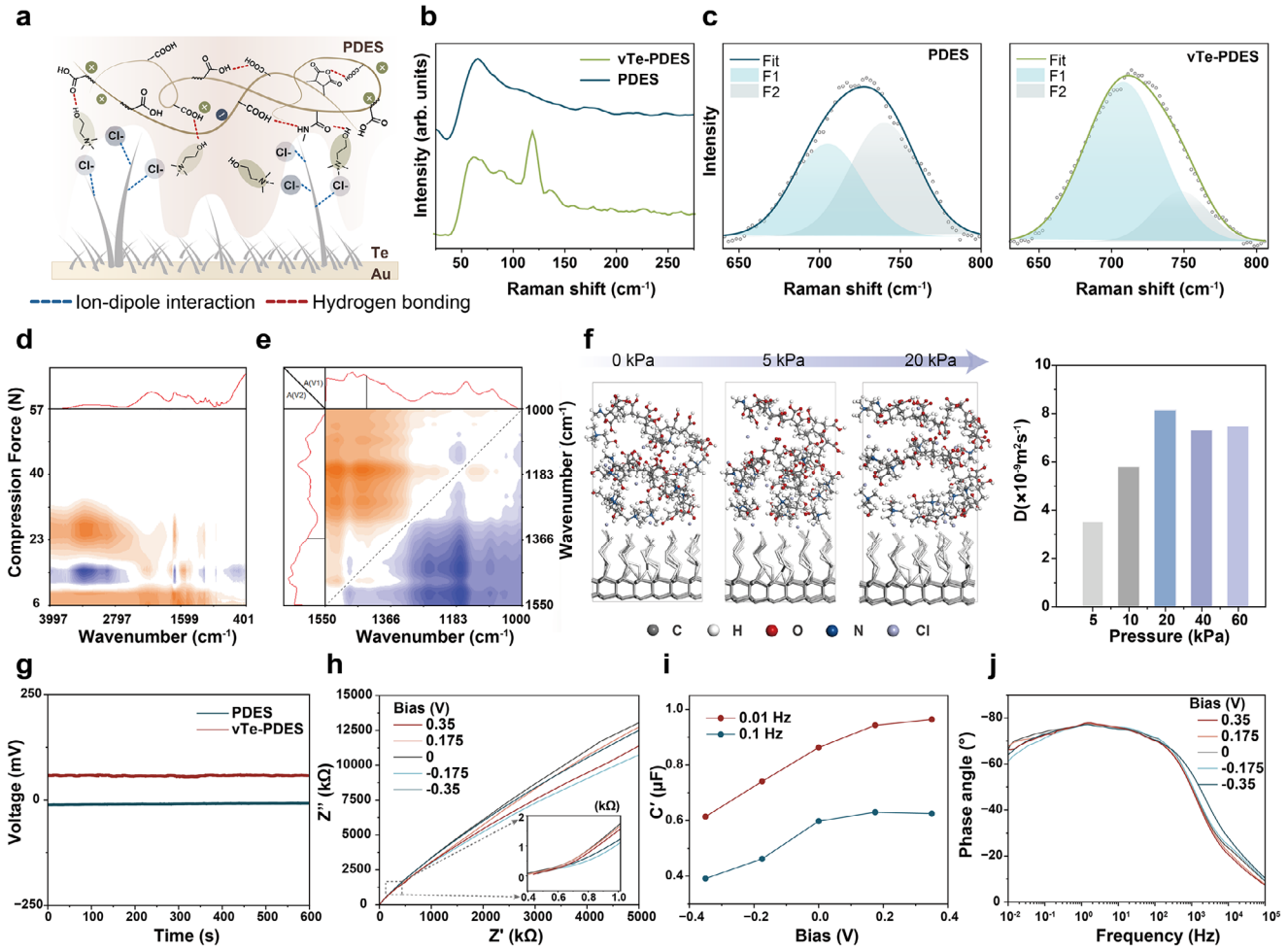


FIGURE 2 | Pressure-gated ion migration driven by dynamic interfacial bonding. (a) Schematic illustration of the supramolecular network, highlighting ion-dipole interactions between Te NWs and Cl^- and the hydrogen bonding within PDES. (b) Raman spectrum of pristine PDES and vTe-PDES composite ionogel. (c) Raman spectral fitting of the –C–N^+– vibration region. (d) PCMW asynchronous spectra under varying pressure. (e) 2D COS asynchronous spectra. In the PCMW and 2D COS spectra, warm colors (yellow) represent positive intensities, while cold colors (blue) represent negative intensities. (f) The snapshots (left) and diffusion coefficients (D) (right) of the motion of $[Ch]^+$ cations under different pressures during molecular dynamics simulations. (g) Open-circuit voltage (OCV) stability of PDES and vTe-PDES. (h) Nyquist plots of the vTe-PDES device recorded at DC bias levels from −0.35 to +0.35 V. Inset: magnified high-frequency region. (i) Interfacial capacitance C′ at 0.01 Hz and 0.1 Hz as a function of DC bias. (j) Corresponding Bode phase plots.

releases further $[Ch]^+$. This pressure-dependent sensitivity of ion migration is further corroborated by MD simulations, which show the $[Ch]^+$ diffusion coefficient increasing substantially from 3.45×10^{-9} m^2 s^{-1} at 5 kPa to 8.17×10^{-9} m^2 s^{-1} at 20 kPa (Figure 2f).

We performed electrochemical measurements to determine how this interface stores and releases charge. The composite ionogel stabilizes at an open-circuit voltage (OCV) of 60 mV, indicating a built-in electric field directed from Te to PDES due to initial $[Ch]^+$ migration, whereas pristine PDES exhibits an OCV of the opposite sign (−10 mV; Figure 2g). Electrochemical impedance spectra recorded from 0.01 Hz to 100 kHz at five DC bias levels (−0.35 to +0.35 V) show no resolvable charge-transfer semicircle at any bias, with the low-frequency branch rising monotonically without curving back toward the real axis (Figure 2h), the signature of an ion-blocking, non-Faradaic interface. The interfacial capacitance C′ increases monotonically with bias, rising steeply from 0 to +0.175 V and leveling off at +0.35 V (Figure 2i) [37]. This saturation indicates a finite density of specific adsorption sites, as expected for the chemically specific Te-Cl^- interaction. The phase minimum remains essentially unchanged across all five bias levels, confirming that near-ideal capacitive behavior persists under both polarities (Figure 2j). The electrochemical stability limits of the electrolyte lie an order of magnitude beyond the voltage generated by the device (Figure S3). Cyclic voltammograms recorded within the operating window (±0.1 V) are quasi-rectangular and featureless at scan rates from 5 to 100 mV s^{-1}, and fifty consecutive cycles retain 98.5% of the initial current (Figure S4).

Together with the spectroscopic evidence above, these results identify the Te-Cl^- interface as a non-Faradaic, site-limited anion reservoir, whose interfacial ion partition governs the pressure-gated migration of $[Ch]^+$.

16163028, 2026, 90, Downloaded from https://advanced.onlinelibrary.wiley.com/doi/10.1002/adfm.78811 by Yu Song - City University Of Hong Kong , Wiley Online Library on [10/11/2026]. See the Terms and Conditions (https://onlinelibrary.wiley.com/terms-and-conditions) on Wiley Online Library for rules of use; OA articles are governed by the applicable Creative Commons License

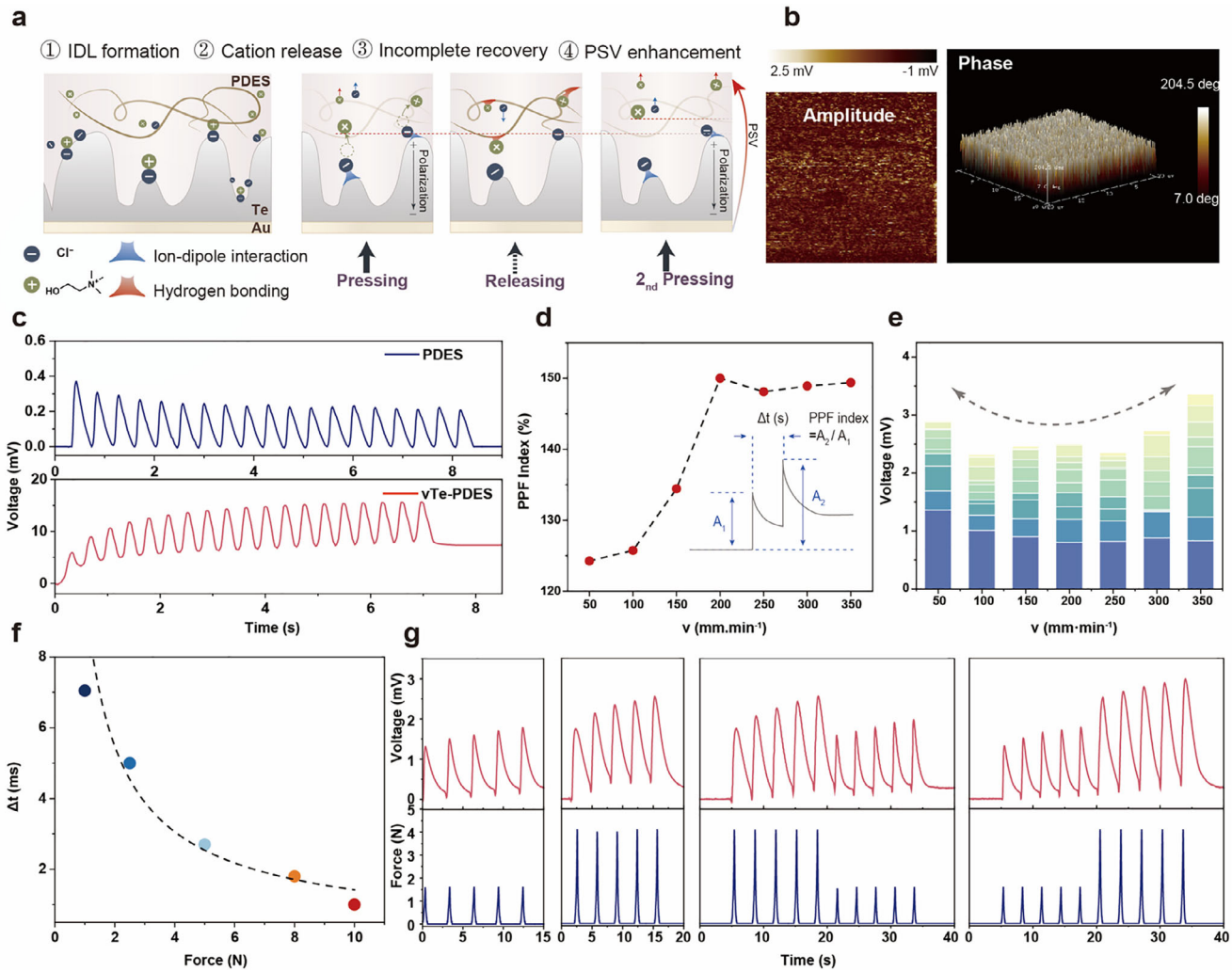


FIGURE 3 | Spatiotemporal synaptic plasticity enabled by the ion-sieving interface. (a) Schematic illustration of the four-stage synaptic transduction mechanism. (b) PFM amplitude and phase images of vertically aligned Te NWs. (c) Voltage-time plots of pristine PDES and vTe-PDES under pulsed pressures. (d) Paired-pulse facilitation (PPF) index as a function of loading rate. (e) Accumulated voltage after ten pulses at different loading rates. Each colored segment represents the voltage increment produced by one pulse, stacked in chronological order. (f) The time required to reach a 1 mV threshold of the composite ionogel under forces of different magnitudes. (g) The voltage response of the vTe-PDES ionogel when two different mechanical stimuli arrive in different sequences.

2.3 | Spatiotemporal Synaptic Plasticity Enabled by the Ion-Sieving Interface

The synaptic piezoelectric voltage from the dynamic ion-sieving interface and asymmetric ion transport channels associated with mechanical touch events occurred as follows: (1) formation of IDL at the Te-PDES interface, (2) pressure-induced directional migration of free $[Ch]^+$, (3) incomplete recovery of $[Ch]^+$ within the polymer network, and (4) renewed migration upon successive stimuli, generating cumulative postsynaptic voltage (PSV) signals, as schematically illustrated in Figure 3a. When pressure was applied to the surface of the vTe-PDES ionogel, $[Ch]^+$ was released from IDL and migrated into the polymer network, establishing a basic piezoionic voltage. Upon cessation of the external driving force, free Cl^- recovers rapidly, whereas $[Ch]^+$ exhibits delayed recovery due to hydrogen bonding modulation and polymer chain relaxation. After that, consecutive stress pulses further amplified the anion-cation concentration gradient via cumulative $[Ch]^+$ accumulation, resulting in the characteristic synaptic STP behavior.

Piezoresponse force microscopy (PFM) evaluates the nanoscale piezoelectric activity in vertically aligned nanowires to support the ion-sieving mechanism (Figure 3b). The nanowires exhibit uniform in-plane distribution and pronounced polarization switching under alternating electric field, confirming the robust polarization that reinforces the interfacial retention of Cl^- and thereby promotes $[Ch]^+$ migration. Under bias-free conditions, characterization of the macroscopic synaptic response reveals distinct behaviors for pristine PDES and the composite ionogel at identical pulsed pressures (Figure 3c). The response of pristine PDES is weak and decays across successive pulses. Without the ion-sieving interface, neither species is selectively immobilized, so the small net separation arising from their mobility difference relaxes promptly upon unloading. In contrast, the composite ionogel induces a voltage elevation at subsequent pulses,

16163028, 2026, 90, Downloaded from https://advanced.onlinelibrary.wiley.com/doi/10.1002/adfm.78811 by Yu Song - City University Of Hong Kong , Wiley Online Library on [10/11/2026]. See the Terms and Conditions (https://onlinelibrary.wiley.com/terms-and-conditions) on Wiley Online Library for rules of use; OA articles are governed by the applicable Creative Commons License

analogous to paired-pulse facilitation (PPF) observed in biological short-term plasticity. Taking the peak amplitude of pristine PDES, 0.37 mV, as a common threshold, the interfacial ion-sieving reduces the time to reach it from 0.43 s in pristine PDES to 0.12 s in the composite. A comparable loss of accumulation occurs when the Te surface is passivated: oxidizing the NW array before infiltration preserves the nanowire geometry while suppressing the facilitation, with A_5/A_1 falling from 2.8 to 1.1 (Figure S5). The specific affinity of the Te surface for Cl^- is therefore what governs the signal accumulation.

To quantify the short-term plasticity, loads of 2.5 N were applied at varying loading rates to analyze the adaptability of asymmetric ion transport channels (Figure 3d). The PPF index is defined as $A_2/A_1 \times 100\%$ (where A_1 and A_2 are the amplitudes of the previous and subsequent response voltages, respectively). As the loading rate increases, the PPF index rises and reaches a saturation plateau, representing the kinetic limit of the ion concentration gradient at a given load. Interestingly, the voltage accumulation exhibits a non-monotonic dependence on stimulation rate, with both slow and ultra-fast pulse rates yielding high final voltage accumulations (Figure 3e). This arises because the loading rate acts in both directions of ion transport by governing the network's compliance. At low loading rates, the polymer chains and dynamic bonds have time to adjust their conformation, and the network remains compliant, so $[Ch]^+$ migrates readily into the bulk, and the first pulse produces a large response. At high loading rates, chain relaxation lags behind the loading, and the network is transiently locked, which restricts the forward migration but hinders the return of $[Ch]^+$ far more effectively, so that a greater proportion of the accumulated voltage is retained between stimuli.

This coupling between cation return and chain dynamics originates from hydrogen bonding of the $[Ch]^+$ hydroxyl group to the network, which anchors the cations to the polymer chains and links their backflow to segmental motion. The decisive role of hydrogen bonding in this retention was confirmed by replacing ChCl with equimolar TMACl, whose cation carries the same charge and a comparable size but lacks the hydroxyl group. The first-pulse amplitude increases from 7.5 to 14.8 mV, consistent with faster cation migration once the hydrogen-bond drag is removed, yet A_5/A_1 falls from 2.8 to 1.2 (Figure S6). Removing this anchoring therefore accelerates cation migration in both directions, and the accumulation is lost even though the ion-sieving interface is unchanged. The carrier concentration was further examined as a separate variable by adjusting the ChCl content over 0.25× to 2× the nominal amount (Figure S7). The accumulated voltage peaks at the nominal composition, whereas A_5/A_1 decreases monotonically as ChCl content increases, consistent with the finite density of Cl^- adsorption sites on the Te surface. The retention time t_{50} remains unchanged across the series, confirming that retention is determined by the polymer network rather than by the carrier concentration. Furthermore, higher mechanical pressures significantly accelerate the release of interfacial cations, drastically shortening the time required to reach a specific voltage threshold (Figure 3f).

Beyond modulation by loading rate and force, the tactile synapse demonstrates advanced capabilities for encoding temporal information. When subjected to two individual stimuli consisting of five spike trains, responses depend on the number and strength of spikes in each stimulus. When subjected to sequential stimuli of varying intensities (1 and 4N), the ionogel successfully recognizes distinct temporal sequences and yields asymmetric response patterns (Figure 3g). Notably, a prior low-strength stimulus primes the network, causing a subsequent high-strength stimulus to generate a significantly amplified response (~3 mV) that exceeds the output of an isolated high-strength event (2.5 mV). This associative learning behavior proves the device's capability to emulate the spatiotemporal complexity of biological neuromorphic systems, providing a solid foundation for environmentally adaptive tactile recognition.

2.4 | Viscoelastic Ion-Trapping and Autonomous Mechanical Adaptability

Serving as the ion-conducting matrix for the tactile synapse, PDES ionogel exhibits viscoelastic properties that govern cation relaxation dynamics. Cyclic compression tests reveal pronounced viscoelastic behavior attributed to the entropic elasticity of polymer chains and abundant dynamic non-covalent bonds (Figure 4a). Hysteresis loops expanded significantly with increasing loading rates, indicating reversible dissociation of hydrogen bonds and ion-dipole interactions to dissipate energy during deformation [38, 39]. The material exhibits strong strain-rate dependence, with Young's modulus increasing monotonically from ~1.5 to 28 MPa as the loading rate increased from 10 to 60 mm min^{-1} (Figure 4b). This pronounced strain-rate stiffening is well rationalized by the Standard Linear Solid (SLS) model [40, 41]. At low strain rates, molecular chains and dynamic bonds within PDES undergo sufficient conformational adjustment, resulting in a compliant network. Conversely, at high strain rates, bond dissociation and chain relaxation lag behind external loading, effectively "locking" the network. This mechanical hysteresis creates a temporal window for ion trapping, where the delayed network recovery physically constrains cation backflow.

To quantify the specific relaxation timescales driving this memory effect, time-temperature superposition (TTS) analysis was conducted. The obtained rheological relaxation spectra reveal the two distinct relaxation modes: slow relaxation at 0.97 s and fast relaxation at 0.03 s, linked to polymer segmental movement and dynamic bond dissociation/reconstruction, respectively [42] (Figure 4c). Since ion transport is coupled with polymer segment relaxation, the $[Ch]^+$ recovery rate is governed by the slow relaxation mode. This coupling was verified directly by holding the device at a fixed compressive strain for different durations before unloading (Figure S8). The recovery time t_{50}, defined as the interval required for the voltage to fall to half its value at the moment of unloading, lengthens from 0.40 to 2.07 s as the hold is extended from 0.1 to 60 s, with the transition occurring between 1 and 10 s, the range containing the slow relaxation mode. The electrical recovery, therefore, follows the timescale of segmental matrix relaxation, which maintains the ion concentration gradient during stimulation intervals and underlies sustained synaptic facilitation. Consistently, the device's bulk resistance decreases from 397 to 166 Ω between 20°C and 50°C (Figure S9), reflecting faster segmental motion in the network and correspondingly higher ion mobility.

16163028, 2026, 90, Downloaded from https://advanced.onlinelibrary.wiley.com/doi/10.1002/adfm.78811 by Yu Song - City University Of Hong Kong , Wiley Online Library on [10/11/2026]. See the Terms and Conditions (https://onlinelibrary.wiley.com/terms-and-conditions) on Wiley Online Library for rules of use; OA articles are governed by the applicable Creative Commons License

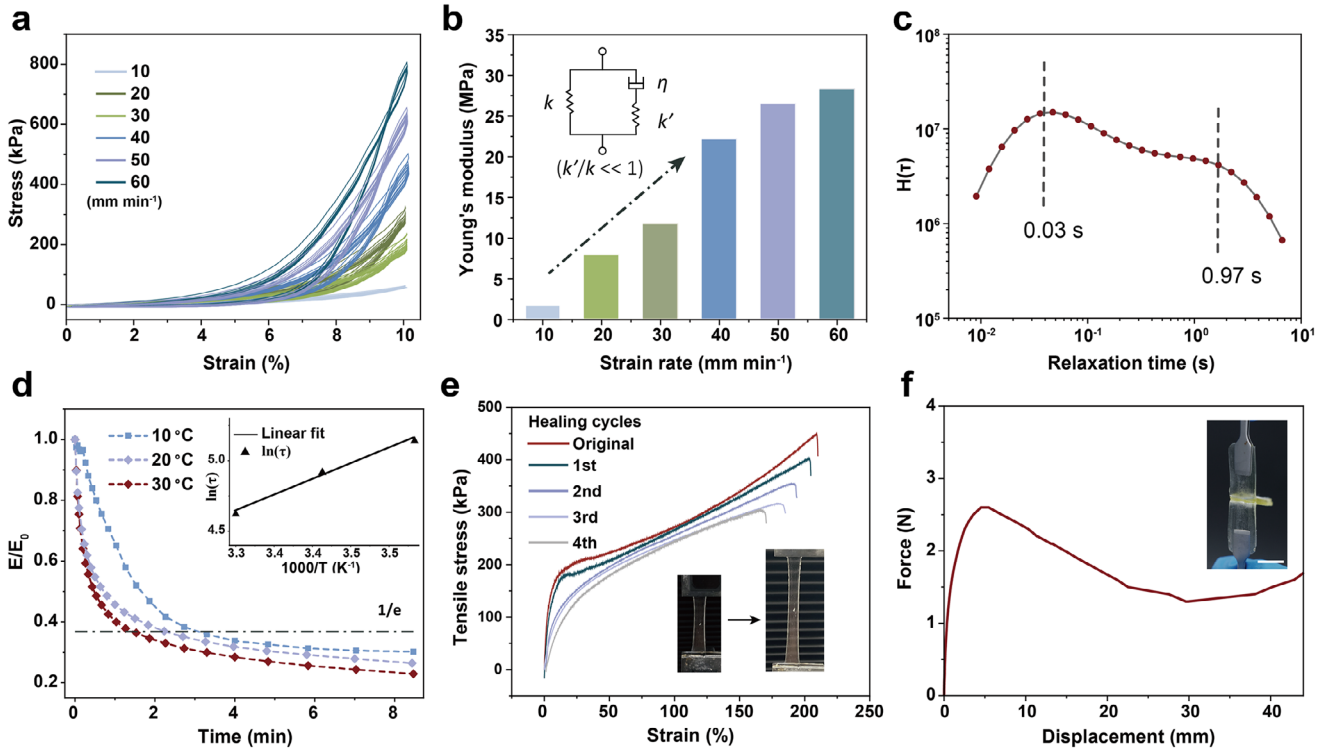


FIGURE 4 | Viscoelastic ion-trapping and autonomous mechanical adaptability. (a) Cyclic compression stress-strain curves of PDES ionogel. The samples were subjected to ten cycles of cyclic loading at varying compressive rates ranging from 10 to 60 mm min^{-1}. (b) Strain-rate dependence of Young's modulus. Inset: Standard Linear Solid (SLS) model illustrating the stiffening mechanism. (c) Relaxation time spectrum of the pristine PDES elastomer. (d) Stress relaxation curves at different temperatures. Inset: Arrhenius fit for activation energy calculation. (e) Tensile stress-strain curves of the original and healed samples. (f) The 180° peeling force-displacement curve. Inset: Photograph during test. Scale bar: 10 mm.

The dynamic supramolecular network responsible for viscoelastic relaxation also endows the ionogel with intrinsic flexibility and remarkable self-healing capabilities. A low glass-transition temperature (T_g) of 6.38°C (Figure S9a) ensures high chain mobility at room temperature, enabling the ionogel to withstand severe bending and twisting deformations without fracture (Figure S10a). The stress-relaxation curves follow a classic exponential Maxwellian decline, yielding an apparent activation energy (E_a) of 267.86 kJ mol^{-1} for the cross-linking network, as determined from the Arrhenius equation, indicating the strong intermolecular interactions coexisting with dynamic reversibility (Figure 4d). When subjected to cyclic shear strains ranging from 0.1% to 1000%, the storage modulus (G') and loss modulus (G'') rapidly recover at small strains, indicating the successful reversibility and cyclic stability of the non-covalent crosslinking network (Figure S10b).

The dynamic bonds also enable autonomous healing. After healing at ambient temperature for 1 h, the compression response and tensile fracture behavior of the self-healed sample were nearly identical to those of the original sample (Figure 4e and Figure S10c), with a self-healing efficiency of 91.8% calculated from tensile toughness. Over four successive cutting-healing cycles, this efficiency decreases to 60.1%, whereas the synaptic response reaches approximately 18 mV after five pulses for all healed samples (Figure S11). Restoring load-bearing capability requires chain interdiffusion and entanglement across the fracture surface, which becomes progressively less complete with repeated cutting. In contrast, ion-conducting pathways are re-established once molecular-scale contact is restored, preserving the mechanoreceptor's synaptic function. Beyond bulk recovery, 180° peel tests were conducted to investigate the reactivity of free dynamic bonds on the ionogel surface. The intrinsic self-adhesion interfacial toughness exceeds 363.6 J m^{-2}, ensuring tight interfacial bonding during deformation and preventing signal distortion for wearable integration (Figure 4f).

The solvent-free composition also confers environmental stability. Unlike hydrogels, which lose water and shrink in open air within 48 h, the PDES elastomer incorporated with $[Ch]^+[Cl]^-$ ion pairs maintains its original shape (Figure S12). The bare ionogel further resists direct immersion, with a mass retention above 95% after 10 min in tap water, artificial sweat, rainwater or anhydrous ethanol, and above 78% after 24 h (Figure S13). At the device level, the open-circuit voltage remains at 60 mV over 24 h of continuous operation while the ambient temperature and humidity vary (Figure S14). These combined mechanical and environmental stabilities ensure signal fidelity and long-term reliability for complex human-machine interaction scenarios.

2.5 | Bias-Free Tactile Perception for In Situ Rehabilitation Monitoring

Leveraging the tactile synaptic processing capability and mechanical adaptability of the vTe-PDES ionogel, we developed a personalized wearable electronic skin for comprehensive assessment of finger rehabilitation. We focused on three critical functional

16163028, 2026, 90, Downloaded from https://advanced.onlinelibrary.wiley.com/doi/10.1002/adfm.78811 by Yu Song - City University Of Hong Kong , Wiley Online Library on [10/11/2026]. See the Terms and Conditions (https://onlinelibrary.wiley.com/terms-and-conditions) on Wiley Online Library for rules of use; OA articles are governed by the applicable Creative Commons License

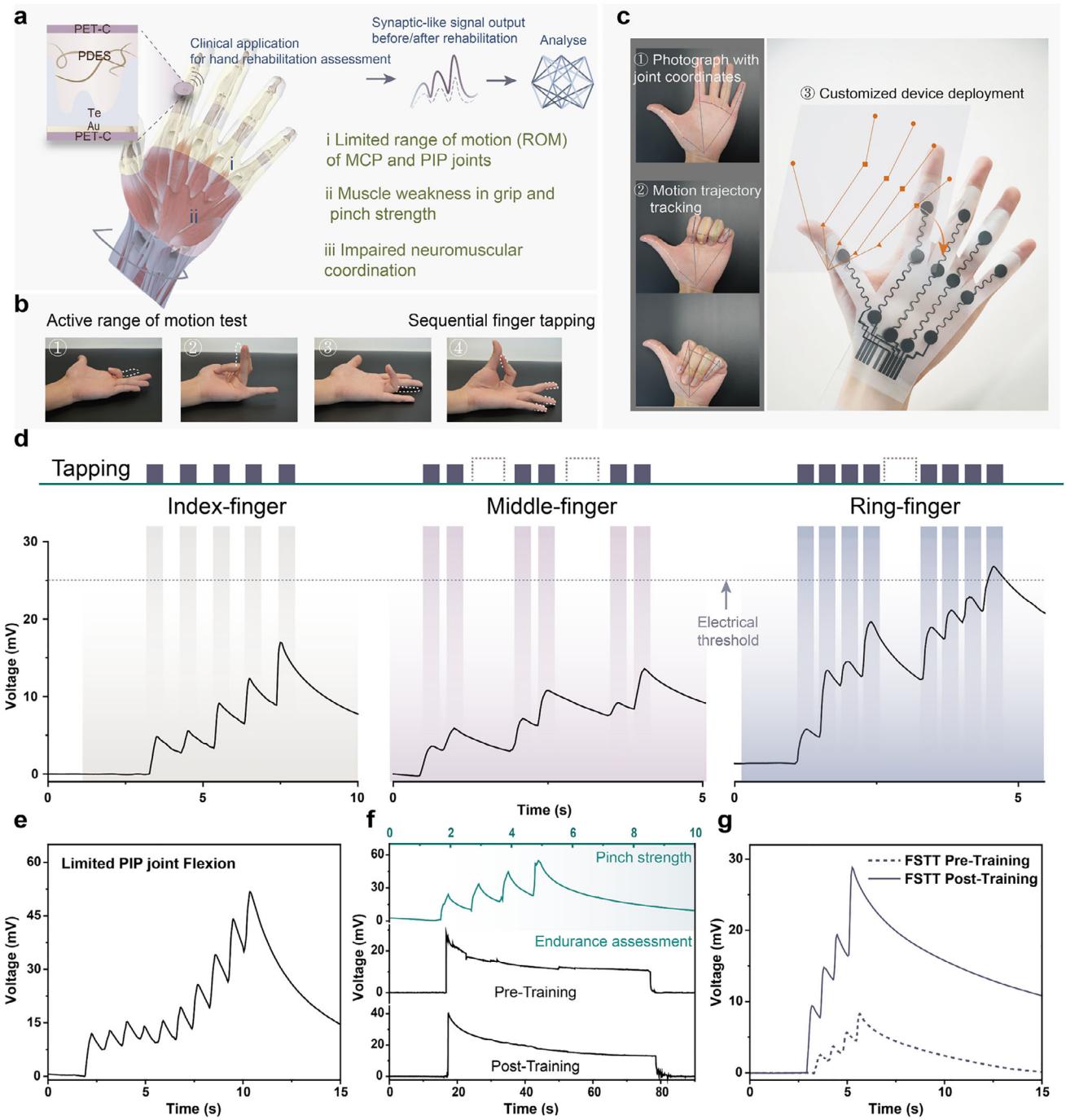


FIGURE 5 | Bias-free tactile perception for in situ rehabilitation monitoring. (a) Schematic illustration of the device integrated with a hand for post-injury deficits monitoring. (b) Rehabilitation tasks performed for assessment: (1-2) ROM test via MCP/PIP flexion and extension; (3) Single-joint flexion; (4) Pinch test and sequential finger tapping for dexterity assessment. (c) Personalized device deployment pipeline. Computer vision algorithms identify anatomical landmarks (1) and motion trajectories (2) to optimize sensor placement (3) for individual patients. (d) Synaptic facilitation during repetitive tapping tasks executing movements (2) depicted above. A rehabilitation benchmark threshold (dotted line) is established. (e) Monitoring of PIP joint flexion under limited ROM conditions. (f) Assessment of pinch strength and muscle fatigue resistance. Top: Signal accumulation during pulsed finger pinch. Middle/Bottom: Comparison of signal decay during sustained contraction pre- and post-rehabilitation training. (g) Evaluation of neuromuscular coordination using the FSTT.

metrics essential for daily activities (e.g., typing, grasping): joint range of motion (ROM), grip endurance, and neuromuscular coordination [43, 44] (Figure 5a). By integrating the Te-PDES sensors onto specific metacarpophalangeal (MCP) and proximal interphalangeal (PIP) joints, as well as palm contact points, the system captures dynamic biomechanical signals associated with the designed rehabilitation tasks (Figure 5b). The system comprises 13 individual devices, in which the postsynaptic voltage after five identical pulses is 19.28 ± 0.57 mV, and the facilitation ratio A5/A1 is 1.82 ± 0.07, corresponding to coefficients of

16163028, 2026, 90, Downloaded from https://advanced.onlinelibrary.wiley.com/doi/10.1002/adfm.78811 by Yu Song - City University Of Hong Kong , Wiley Online Library on [10/11/2026]. See the Terms and Conditions (https://onlinelibrary.wiley.com/terms-and-conditions) on Wiley Online Library for rules of use; OA articles are governed by the applicable Creative Commons License

variation of 3.0% and 3.6%, respectively (Figure S15). Hand recognition algorithms, combined with image analysis, were employed to identify anatomical landmarks, enabling the personalized deployment of the e-skin with optimized sensor coordinates to ensure precise finger contact (Figure 5c and Figure S16).

The synaptic facilitation was first exploited in repetitive tapping tasks (Figure 5d). We evaluated the piezoelectric data from the index, middle, and ring fingers executing movements 1 and 2 (Figure 5b) at various rhythms (Figure S17). A rehabilitation benchmark threshold of 25 mV was established to evaluate performance. Notably, the ring finger, executing taps at a higher frequency, surpassed this threshold after eight stimuli due to rapid signal accumulation. In contrast, the index and middle fingers, tapping at slower rhythms, remained below the threshold despite five to six stimuli. This demonstrates that the device does not merely detect motion but quantifies movement frequency and intensity directly through material-level synaptic potentiation. For patients with severe impairment limiting full fist closure, single-joint flexion served as a surrogate metric. The PIP sensor on the index finger generated a robust signal (>50 mV) after ten cycles, confirming high sensitivity even under constrained ROM (Figure 5e).

We further quantified muscle endurance by extracting the voltage evolution during a static thumb-index pinch grip test (Figure 5f). Compared with pre-training, post-training signals showed a ~40% increase in initial amplitude, indicating a recovery in grip strength. The signal decay rate during sustained contraction was markedly lower in the post-training group than in the pre-training state, reflecting enhanced fatigue resistance and muscle stability. Finally, the device's temporal memory was used to evaluate neuromuscular coordination using the Finger Sequential Tapping Test (FSTT) (Figure 5g). The post-training signal profile showed significantly higher voltage accumulation and a higher rate of increase than in the pre-training state, indicating improved inter-digit synchronization and tendon load-bearing capacity. For quantitative comparison across different fingers or individuals, the first-pulse amplitude and the subsequent accumulation, which reflect the applied force and the inter-stimulus interval, respectively, could be extracted separately from a single trace to enable more refined rehabilitation assessment. Collectively, these demonstrations validate the monolithic piezoionic synapse as a powerful paradigm for in-sensor kinematic tracking. By eliminating the need for continuous external biasing or complex intermediate transduction, this self-powered architecture paves the way for energy-efficient, associative-learning-enabled electronic skins for continuous physical monitoring.

3 | Discussion

In summary, we present a monolithic, piezoionic tactile synapse that autonomously modulates synaptic plasticity in response to mechanical stimuli. The underlying computational mechanism arises from a dynamic ion-sieving interface regulated by the piezoelectric polarization of Te NWs. It is seamlessly coupled with the viscoelastic memory of the polymer matrix. This synergy induces a robust ion-trapping effect for temporal signal accumulation. Unlike conventional transistor-based architectures, this bias-free strategy modulates spatiotemporal ion transport without external power, thereby circumventing the energy constraints and structural complexities of traditional neuromorphic arrays. Concurrently, the abundant non-covalent dynamic network endows the ionogel with intrinsic flexibility and autonomous self-healing, mitigating the mechanical mismatch and fragility typical of conventional electronic skins. By leveraging its STP and mechanical adaptivity, we successfully demonstrated a personalized wearable system for hand rehabilitation monitoring, offering reliable tracking of joint motion quality, muscle strength/endurance, and neuromuscular coordination. Ultimately, this work establishes a material-level paradigm for in-sensor neuromorphic computing, offering a scalable and energy-efficient route toward autonomous intelligent skins for advanced human-machine interfaces and healthcare diagnostics.

4 | Experimental Section

4.1 | Materials

Acrylic acid (AA, AR), (Z)-4-(Methylamino)-4-0xobut-2-Enoic Acid (NMA, AR), maleic anhydride (MA, AR) and poly (ethylene glycol) diacrylate (PEG(200)-DA) were purchased from Shanghai Macklin Biochemical Co. Choline chloride (ChCl, 99%), 2-hydroxy-4-(2-hydroxyethoxy)-2-methylpropiophenone (photoinitiator 2959, ≥98%) and tetramethylammonium chloride (TMACl, ≥98%) were bought from Shanghai Titan Scientific Co. Tellurium (99.99% metal basis, 200 mesh) was purchased from Sigma-Aldrich Co. Sodium chloride (NaCl, AR), L-lactic acid (AR) and urea (AR) were purchased from Shanghai Macklin Biochemical Co. All chemicals were used as received.

4.2 | Preparation of the Te NWs

Tellurium NWs were synthesized via a physical vapor deposition (PVD) method in a dual-zone horizontal tube furnace equipped with a 1-inch inner diameter quartz tube. A quartz tube containing 300 mg of tellurium powder was placed in the high-temperature zone (source zone), heated to 500°C to vaporize the precursor. The growth substrate, a polyimide (PI) film pre-deposited with a 10 nm Cr adhesion layer and a 40 nm Au catalyst layer, was positioned in the low-temperature (growth) zone at 100°C. Before heating, the system was purged with argon gas (200 SCCM) for 30 min to remove residual oxygen. During growth, the argon flow was reduced to 50 standard cubic centimeters per minute (SCCM), and the system pressure was maintained at 100 Torr. The tellurium vapor was transported to the substrate, and nanowire growth was maintained for 30 min. For the passivated control, the as-grown Te NWs were heated in air at 150°C for 1 h before infiltration with the PDES precursor, yielding the oxidized array denoted oTe.

4.3 | Preparation of the Ionogels

The precursor for the PDES was prepared by mixing AA, NMA, MA, and ChCl (molar ratio AA: NMA: MA: ChCl = 30: 2: 3: 10) in a sealed flask. The mixture was stirred and heated to 85°C for 2 h to form a colorless, homogeneous solution, driven by extensive hydrogen-bonding networks. Subsequently, 0.1 mol% of

16163028, 2026, 90, Downloaded from https://advanced.onlinelibrary.wiley.com/doi/10.1002/adfm.78811 by Yu Song - City University Of Hong Kong , Wiley Online Library on [10/11/2026]. See the Terms and Conditions (https://onlinelibrary.wiley.com/terms-and-conditions) on Wiley Online Library for rules of use; OA articles are governed by the applicable Creative Commons License

photoinitiator 2959 and 0.1 mol% of crosslinker PEGDA (relative to the total moles of monomers) were added to the mixture. The resulting solution was sonicated in a water bath until a uniform dispersion was achieved, denoted as PDES in this work. The formed ionogel precursor was then stored in a vacuum desiccator with silica gel for further use. For the salt-content series, precursors were prepared using the same procedure, with the ChCl content adjusted to 0.25×, 0.5×, and 2× the nominal molar ratio given above. For cation control, ChCl was replaced with an equimolar amount of TMACl, with all other components and conditions remaining identical.

4.4 | Device Fabrication

The PDES precursor was drop-cast onto the surface of the vertically grown Te NWs and allowed to infiltrate for 5 min to establish interfacial supramolecular interactions. Subsequently, the coated substrate was spin-coated at 1000 rpm for 1 min to ensure a uniform film thickness. Polymerization was initiated by exposing the composite to 365 nm UV light in a dark chamber for 30 min to ensure complete polymerization, yielding the final composite denoted as vTe-PDES. For control experiments and characterization of adhesion, mechanical properties, and environmental stability, the PDES precursor was poured into polytetrafluoroethylene (PTFE) molds and polymerized under identical UV curing conditions.

4.5 | Characterizations and Measurement

Scanning electron microscopy (SEM) images were acquired using a Thermo Fisher Apreo 2 system. Raman spectra were collected using a WITec alpha300 R system with a 532 nm excitation laser over a range of 400–4000 cm^{-1}. Fourier transform infrared (FTIR) spectra were recorded in attenuated total reflectance (ATR) mode (4000–800 cm^{-1}) using a PerkinElmer FTIR spectrometer. To investigate the pressure response, pressure-dependent ATR-FTIR spectra were recorded for 1 mm-thick piezoionic elastomer films under varying compressive loads. X-ray photoelectron spectra were recorded on a Thermo SCIENTIFIC Nexsa spectrometer with Al Kα radiation.

The glass transition temperature (T_g) of the PDES was determined via dynamic mechanical analysis (DMA) using a TA Instruments Q800 analyzer. Temperature ramp tests were conducted from −55°C to 105°C at a heating rate of 5°C min^{-1} and a frequency of 1 Hz. Stress-relaxation tests were performed at a constant strain of 1% at 10°C, 20°C, and 30°C. Rheological properties were investigated using a Thermo Scientific HAAKE MARS 60 modular advanced rheometer equipped with a 20 mm parallel-plate geometry. Strain sweep measurements were conducted over an oscillatory strain range of 0.1% to 1000%. Frequency-sweep tests were performed from 0.01 to 100 Hz at a fixed strain amplitude of 0.1%, with temperature intervals of 10°C spanning −10°C to 60°C. Finally, Time-Temperature Superposition (TTS) analysis was applied to construct master curves and derive the relaxation time spectra.

Molecular dynamics (MD) simulations were performed using the Forcite module in Materials Studio to investigate the transport behavior of $[Ch]^+$ ions under mechanical compression. A molecular model of a single repeating unit composed of AA, MAH, and NAM was first built and energy-minimized. The periodic cells containing AA/NAM/MAH/ChCl-type PDES and vertically grown Te NWs were then constructed and subjected to geometry optimization. After that, an NPT MD simulation was performed to achieve a realistic model density. To mimic the tactile stimulus, production simulations with an NPT ensemble were carried out, in which stress in the Z-axis at different values (0, 5, 10, 20, 40, and 60 kPa) was applied to the model. The COMPASS force field was employed to describe interatomic interactions, and the atomic charges were retained from the equilibrated configurations. Before the production runs, energy minimization was conducted using the Smart Minimizer algorithm to relax the structure. In the simulation procedure, long-range electrostatic interactions were calculated using the Ewald summation method with a high accuracy of 1×10^{-5} kcal mol^{-1} and a buffer width of 0.5 Å. Van der Waals interactions were treated using an atom-based summation method with a cubic spline truncation function. A cutoff distance of 18.5 Å was applied, with a spline width of 1.0 Å, and tail corrections for long-range interactions were enabled. The trajectories of $[Ch]^+$ ions were recorded to analyze the pressure-dependent ionic migration. The diffusion coefficients of $[Ch]^+$ under stress were calculated by the Einstein relationship, which is expressed as

$$D_i = \frac{1}{6} \lim_{t\to\infty} \frac{d}{dt} \sum_{i=1}^{N_a} \left\langle \left(r_i(t) - r_i(0)\right)^2 \right\rangle$$

where N_a is the number of diffusing atoms α, $(r_i(t) - r_i(0))$ is the mean square displacement (MSD) of the atom i, $r_i(t)$ and $r_i(0)$ denote the position vector of atom i at time t and the initial time 0.

Open-circuit potential-time (OCPT) curves were recorded using a CHI 760E electrochemical workstation. The long-term stability was assessed by continuously recording the open-circuit voltage for 24 h at room temperature, with ambient temperature and relative humidity logged over the same period. Conductive carbon cloth with a thickness of 0.33 mm was used as the electrode. In the measurement configuration, the PDES layer was connected to the working electrode, and the Te NW array to the reference electrode. Cyclic voltammograms were measured on a CHI 1140D instrument. Wide-window scans were recorded over −1.2 to +1.2 V at 5, 10, and 50 mV s^{-1}, and operating-window scans over ±0.1 V at 5, 10, 20, 50, and 100 mV s^{-1}, with fifty consecutive cycles recorded at 100 mV s^{-1}. Electrochemical impedance spectroscopy was performed on the CHI 760E workstation from 0.01 Hz to 100 kHz with an AC amplitude of 5 mV, at DC bias levels of −0.35, −0.175, 0, +0.175, and +0.35 V. Temperature-dependent impedance spectra were recorded from 20°C to 50°C. The bulk resistance R_b was obtained by linear extrapolation of the three highest-frequency points to the real axis. The interfacial capacitance C' was obtained from the complex-capacitance representation of the impedance data

$$C'(\omega) = \frac{-Z''}{\omega\left(Z'^2 + Z''^2\right)}$$

16163028, 2026, 90, Downloaded from https://advanced.onlinelibrary.wiley.com/doi/10.1002/adfm.78811 by Yu Song - City University Of Hong Kong , Wiley Online Library on [10/11/2026]. See the Terms and Conditions (https://onlinelibrary.wiley.com/terms-and-conditions) on Wiley Online Library for rules of use; OA articles are governed by the applicable Creative Commons License

where Z' and Z'' are the real and imaginary parts of the impedance and ω is the angular frequency. C' was evaluated at 0.01 and 0.1 Hz (Figure S18).

Piezoresponse force microscopy (PFM) measurements were conducted using Bruker Dimension Icon and Asylum Research Cipher ES systems equipped with conductive probes (SCM-PIT-V2). Amplitude and phase signals were acquired during a DC bias voltage sweep from −2 to +2 V. The real-time piezoionic sensing performance of the as-prepared ionogel was recorded using a DAQ2610 data acquisition and multimeter system. For all pressure-dependent measurements, the ionogel was assembled with PET-supported carbon electrodes (PET-C), prepared by coating carbon paste onto PET films and curing the coated films before assembly. For the strain-hold measurements, the device was compressed to a fixed strain rate of 100 mm min^{-1}, held for 0.1, 1, 10, or 60 s, and then unloaded. The recovery time t_{50} was defined as the interval required for the voltage to fall to half its value at the moment of unloading. All compositional and control comparisons, including the TMACl and ChCl-content series, the oTe-PDES control, the repeated-healing tests, and the device-uniformity measurements, were performed at 10 N and 200 mm min^{-1}. For the rehabilitation assessments, pre- and post-training signals were recorded from the same finger performing the same task. The effective piezoelectric coefficient of Te NWs, pristine PDES, and the composite films was evaluated using a ZJ-3AN quasi-static d_{33} measuring meter.

Mechanical properties were evaluated using an Instron Series 34SC-1 UTM System (USA) equipped with a 1000 N load cell. The samples for mechanical compression tests had a diameter of 10 mm and a thickness of 1 mm. Compression cycle testing was performed at rates of 10–60 mm min^{-1}, with a strain of 10%. For self-healing mechanical property tests, the PDES sample was first cut in half with a razor blade. Then the two fresh sections were immediately brought together to fully heal at room temperature. Tensile tests were conducted on specimens with a gauge length of 15 mm, a width of 2 mm, and a thickness of 1.0 mm. The self-healing efficiency (η) in this work was defined as the proportion of toughness restored relative to the original one. Adhesion strength was quantified via 180° peel tests. Before testing, two rectangular strips (15 × 0.5 × 0.1 cm) were laminated under a 1000 g load for 45 min, then delaminated at a constant rate of 50 mm min^{-1}. To evaluate the solvent resistance, bare samples were immersed in tap water, artificial sweat, rainwater, and anhydrous ethanol at room temperature. Artificial sweat was prepared by dissolving NaCl (5 g L^{-1}), L-lactic acid (1 g L^{-1}), and urea (1 g L^{-1}) in deionized water and adjusting the pH to 6.5 with aqueous ammonia. After 10 min and 24 h of immersion, the samples were removed, photographed, and dried under vacuum at 60°C. The mass retention was calculated as the ratio of the dried mass after immersion to the sample's initial mass.

Author Contributions

N.W. structured and designed the experiments. Y.Y., M.D., and Y.Z. helped with the synthesis and characterization of vTe-PDES ionogel. N.W. and M.G. performed device fabrication. N.W. and Y.Z. finished the simulation. N.W. and J.Z. performed the Rheological tests. W.G., H.P., B.L., and Q.Q. helped with electrical measurements and data analysis. Y.Y., M.D., and Y.Z. helped revise the paper. All authors discussed the results and commented on the manuscript.

Acknowledgements

This research was financially supported by the Research Grants Council of the Hong Kong Special Administrative Region, China (Project No. CRS_CityU101/24), the Innovation and Technology Fund (MHP/044/23) from the Innovation Technology Commission of the Hong Kong Special Administrative Region, China, the Science Technology and Innovation Committee of Shenzhen Municipality (Project No. JCYJ20230807114910021), the Guangdong Basic and Applied Basic Research Fund (Project no. 2024A1515011922), and the National Natural Science Foundation of China (Project no. 62501507).

Conflicts of Interest

The authors declare no conflicts of interest.

Data Availability Statement

The data of this study are available within the article and the Supplementary Information file. All raw data generated during the current study are available from the corresponding author upon request. Source data are provided with this paper.

References

1. Y. Chen, H. Wang, Y. Yao, Y. Wang, C. Ma, and P. Samorì, "Synaptic Plasticity Powering Long-Afterglow Organic Light-Emitting Transistors," *Advanced Materials* 33 (2021): 2103369, https://doi.org/10.1002/adma.202103369.

2. S. Chen, M. R. Mahmoodi, Y. Shi, et al., "Wafer-Scale Integration of Two-Dimensional Materials in High-Density Memristive Crossbar Arrays for Artificial Neural Networks," *Nature Electronics* 3 (2020): 638–645, https://doi.org/10.1038/s41928-020-00473-w.

3. Z. Li, S. K. Myers, J. Xiao, et al., "Neuromorphic Ionic Computing in Droplet Interface Synapses," *Science Advances* 11 (2025): adv6603, https://doi.org/10.1126/sciadv.adv6603.

4. D. Kudithipudi, C. Schuman, C. M. Vineyard, et al., "Neuromorphic Computing at Scale," *Nature* 637 (2025): 801–812, https://doi.org/10.1038/s41586-024-08253-8.

5. S.-H. Woo, E. A. Lumpkin, and A. Patapoutian, "Merkel Cells and Neurons Keep in Touch," *Trends in Cell Biology* 25 (2015): 74–81, https://doi.org/10.1016/j.tcb.2014.10.003.

6. Z. Lei and P. Wu, "A Highly Transparent and Ultra-Stretchable Conductor With Stable Conductivity During Large Deformation," *Nature Communications* 10 (2019): 3429, https://doi.org/10.1038/s41467-019-11364-w.

7. J.-H. Youn, S.-Y. Jang, I. Hwang, Q. Pei, S. Yun, and K.-U. Kyung, "Skin-Attached Haptic Patch for Versatile and Augmented Tactile Interaction," *Science Advances* 11 (2025): adt4839, https://doi.org/10.1126/sciadv.adt4839.

8. B. Kang, N. Zavanelli, G. N. Sue, et al., "A Flexible Skin-Mounted Haptic Interface for Multimodal Cutaneous Feedback," *Nature Electronics* 8 (2025): 818–830, https://doi.org/10.1038/s41928-025-01443-w.

9. C. Kaspar, B. J. Ravoo, W. G. van der Wiel, S. V. Wegner, and W. H. P. Pernice, "The Rise of Intelligent Matter," *Nature* 594 (2021): 345–355, https://doi.org/10.1038/s41586-021-03453-y.

10. W. Kim, K. Lee, S. Choi, et al., "Electrochemiluminescent Tactile Visual Synapse Enabling In Situ Health Monitoring," *Nature Materials* 24 (2025): 925–934, https://doi.org/10.1038/s41563-025-02124-x.

11. H. Shim, F. Ershad, S. Patel, et al., "An Elastic and Reconfigurable Synaptic Transistor Based on a Stretchable Bilayer Semiconductor," *Nature Electronics* 5 (2022): 660–671, https://doi.org/10.1038/s41928-022-00836-5.

16163028, 2026, 90, Downloaded from https://advanced.onlinelibrary.wiley.com/doi/10.1002/adfm.78811 by Yu Song - City University Of Hong Kong , Wiley Online Library on [10/11/2026]. See the Terms and Conditions (https://onlinelibrary.wiley.com/terms-and-conditions) on Wiley Online Library for rules of use; OA articles are governed by the applicable Creative Commons License

12. S. Wang, X. Chen, C. Zhao, et al., "An Organic Electrochemical Transistor for Multi-Modal Sensing, Memory and Processing," *Nature Electronics* 6 (2023): 281–291, https://doi.org/10.1038/s41928-023-00950-y.

13. K. He, C. Wang, Y. He, J. Su, and X. Chen, "Artificial Neuron Devices," *Chemical Reviews* 123 (2023): 13796–13865, https://doi.org/10.1021/acs.chemrev.3c00527.

14. C. Wan, G. Chen, Y. Fu, et al., "An Artificial Sensory Neuron With Tactile Perceptual Learning," *Advanced Materials* 30 (2018): 1801291, https://doi.org/10.1002/adma.201801291.

15. Y. Kim, A. Chortos, W. Xu, et al., "A Bioinspired Flexible Organic Artificial Afferent Nerve," *Science* 360 (2018): 998–1003, https://doi.org/10.1126/science.aao0098.

16. H. Shim, K. Sim, F. Ershad, et al., "Stretchable Elastic Synaptic Transistors for Neurologically Integrated Soft Engineering Systems," *Science Advances* 5 (2019): aax4961, https://doi.org/10.1126/sciadv.aax4961.

17. L. Q. Guo, J. Wen, L. Q. Zhu, Y. M. Fu, and H. Xiao, "Humidity-Dependent Synaptic Plasticity for Proton Gated Oxide Synaptic Transistor," *IEEE Electron Device Letters* 38 (2017): 1248–1251, https://doi.org/10.1109/LED.2017.2723917.

18. Y. Wang, D. Liu, Y. Zhang, et al., "Stretchable Temperature-Responsive Multimodal Neuromorphic Electronic Skin With Spontaneous Synaptic Plasticity Recovery," *ACS Nano* 16 (2022): 8283–8293, https://doi.org/10.1021/acsnano.2c02089.

19. H. Shim, K. Sim, F. Ershad, et al., "Stretchable Elastic Synaptic Transistors for Neurologically Integrated Soft Engineering Systems," *Science Advances* 5 (2019): aax4961, https://doi.org/10.1126/sciadv.aax4961.

20. M.-K. Kim and J.-S. Lee, "Ferroelectric Analog Synaptic Transistors," *Nano Letters* 19 (2019): 2044–2050, https://doi.org/10.1021/acs.nanolett.9b00180.

21. G. Zhang, C. Ma, X. Wu, et al., "Transparent Organic Nonvolatile Memory and Volatile Synaptic Transistors Based on Floating Gate Structure," *IEEE Electron Device Letters* 43 (2022): 733–736, https://doi.org/10.1109/LED.2022.3164090.

22. H. Han, H. Yu, H. Wei, J. Gong, and W. Xu, "Recent Progress in Three-Terminal Artificial Synapses: From Device to System," *Small* 15 (2019): 1900695, https://doi.org/10.1002/smll.201900695.

23. T. Hannay, A. Larkman, K. Stratford, and J. Jack, "A Common Rule Governs the Synaptic Locus of Both Short-Term and Long-Term Potentiation," *Current Biology* 3 (1993): 832–841, https://doi.org/10.1016/0960-9822(93)90217-C.

24. P. Robin, T. Emmerich, A. Ismail, et al., "Long-Term Memory and Synapse-Like Dynamics in Two-Dimensional Nanofluidic Channels," *Science* 379 (2023): 161–167, https://doi.org/10.1126/science.adc9931.

25. C. Yang and Z. Suo, "Hydrogel Ionotronics," *Nature Reviews Materials* 3 (2018): 125–142, https://doi.org/10.1038/s41578-018-0018-7.

26. D. J. Perkel, S. Hestrin, P. Sah, and R. A. Nicoll, "Excitatory Synaptic Currents in Purkinje Cells," *Proceedings of the Royal Society B: Biological Sciences* 241 (1990): 116–121, https://doi.org/10.1098/rspb.1990.0074.

27. P. E. Schulz and J. C. Fitzgibbons, "Differing Mechanisms of Expression for Short- and Long-Term Potentiation," *Journal of Neurophysiology* 78 (1997): 321–334, https://doi.org/10.1152/jn.1997.78.1.321.

28. M. Pi, H. Wu, W. Li, et al., "Facile Preparation of Polymerizable Deep Eutectic Solvents Under Mild Conditions for Multisensory Ionic Skins," *Small* 21 (2025): 2409754, https://doi.org/10.1002/smll.202409754.

29. N. Wang, X. Yang, and X. Zhang, "Ultrarobust Subzero Healable Materials Enabled by Polyphenol Nano-Assemblies," *Nature Communications* 14 (2023): 814, https://doi.org/10.1038/s41467-023-36461-9.

30. J. Zhang, J. Zhang, Y. Qi, et al., "Room-Temperature Ferroelectric, Piezoelectric and Resistive Switching Behaviors of Single-Element Te Nanowires," *Nature Communications* 15 (2024): 7648, https://doi.org/10.1038/s41467-024-52062-6.

31. J. Gou, H. Bai, X. Zhang, et al., "Two-Dimensional Ferroelectricity in a Single-Element Bismuth Monolayer," *Nature* 617 (2023): 67–72, https://doi.org/10.1038/s41586-023-05848-5.

32. Y. Wang, C. Xiao, M. Chen, et al., "Two-Dimensional Ferroelectricity and Switchable Spin-Textures in Ultra-Thin Elemental Te Multilayers," *Materials Horizons* 5 (2018): 521–528, https://doi.org/10.1039/C8MH00082D.

33. D. Spirito, S. Marras, and B. Martín-García, "Lattice Dynamics in Chiral Tellurium by Linear and Circularly Polarized Raman Spectroscopy: Crystal Orientation and Handedness," *Journal of Materials Chemistry C* 12 (2024): 2544–2551, https://doi.org/10.1039/D3TC04333A.

34. W. Zhu, B. Wu, Z. Lei, and P. Wu, "Piezoionic Elastomers by Phase and Interface Engineering for High-Performance Energy-Harvesting Ionotronics," *Advanced Materials* 36 (2024): 2313127, https://doi.org/10.1002/adma.202313127.

35. R. Geitner, J. Kötteritzsch, M. Siegmann, et al., "Two-Dimensional Raman Correlation Spectroscopy Reveals Molecular Structural Changes During Temperature-Induced Self-Healing in Polymers Based on the Diels–Alder Reaction," *Physical Chemistry Chemical Physics* 17 (2015): 22587–22595, https://doi.org/10.1039/C5CP02151K.

36. H. Wang, H. Liu, Z. Cao, et al., "Room-Temperature Autonomous Self-Healing Glassy Polymers With Hyperbranched Structure," *Proceedings of the National Academy of Sciences* 117 (2020): 11299–11305, https://doi.org/10.1073/pnas.2000001117.

37. P. L. Taberna, P. Simon, and J. F. Fauvarque, "Electrochemical Characteristics and Impedance Spectroscopy Studies of Carbon-Carbon Supercapacitors," *Journal of The Electrochemical Society* 150 (2003): A292, https://doi.org/10.1149/1.1543948.

38. X. Qiu, Q. Cui, Q. Guo, et al., "Strong, Healable, Stimulus-Responsive Fluorescent Elastomers Based on Assembled Borate Dynamic Nanostructures," *Small* 18 (2022): 2107164, https://doi.org/10.1002/smll.202107164.

39. Y. Wang, Q. Guo, G. Su, J. Cao, J. Liu, and X. Zhang, "Hierarchically Structured Self-Healing Actuators With Superfast Light- and Magnetic-Response," *Advanced Functional Materials* 29 (2019): 1906198, https://doi.org/10.1002/adfm.201906198.

40. J. D. Williams and C. R. Deckard, "Advances in Modeling the Effects of Selected Parameters on the SLS Process," *Rapid Prototyping Journal* 4 (1998): 90–100, https://doi.org/10.1108/13552549810210257.

41. S. Li, A. G. Patwardhan, F. M. L. Amirouche, R. Havey, and K. P. Meade, "Limitations of the Standard Linear Solid Model of Intervertebral Discs Subject to Prolonged Loading and Low-Frequency Vibration in Axial Compression," *Journal of Biomechanics* 28 (1995): 779–790, https://doi.org/10.1016/0021-9290(94)00140-Y.

42. V. Bocharova and A. P. Sokolov, "Perspectives for Polymer Electrolytes: A View From Fundamentals of Ionic Conductivity," *Macromolecules* 53 (2020): 4141–4157, https://doi.org/10.1021/acs.macromol.9b02742.

43. M. D. Bland, J. A. Beebe, D. D. Hardwick, and C. E. Lang, "Restricted Active Range of Motion at the Elbow, Forearm, Wrist, or Fingers Decreases Hand Function," *Journal of Hand Therapy* 21 (2008): 268–275, https://doi.org/10.1197/j.jht.2008.01.003.

44. J. Lai, A. Song, K. Shi, Q. Ji, Y. Lu, and H. Li, "Design and Evaluation of a Bidirectional Soft Glove for Hand Rehabilitation-Assistance Tasks," *IEEE Transactions on Medical Robotics and Bionics* 5 (2023): 730–740, https://doi.org/10.1109/TMRB.2023.3292414.

Supporting Information

Additional supporting information can be found online in the Supporting Information section.

Supporting File: adfm78811-sup-0001-SuppMat.pdf.

16163028, 2026, 90, Downloaded from https://advanced.onlinelibrary.wiley.com/doi/10.1002/adfm.78811 by Yu Song - City University Of Hong Kong , Wiley Online Library on [10/11/2026]. See the Terms and Conditions (https://onlinelibrary.wiley.com/terms-and-conditions) on Wiley Online Library for rules of use; OA articles are governed by the applicable Creative Commons License